Chiral modulations and reorientation effects in MnSi thin films

E. A. Karhu,[1] U. K. Rößler,[2] A. N. Bogdanov,[2] S. Kahwaji,[1] B. J. Kirby,[3] H. Fritzsche,[4] M. D. Robertson,[5] C. F. Majkrzak,[3] and T. L. Monchesky[1,*]

[1]*Department of Physics and Atmospheric Science, Dalhousie University, Halifax, Nova Scotia, Canada B3H 3J5*
[2]*Institut für Festkörper- und Werkstoffforschung, IFW Dresden, Postfach 270016, D-01171 Dresden, Germany*
[3]*Center for Neutron Research, NIST, Gaithersburg Maryland 20899, USA*
[4]*National Research Council Canada, Canadian Neutron Beam Centre, Chalk River, Ontario, Canada K0J 1J0*
[5]*Department of Physics, Acadia University, Wolfville, Nova Scotia, Canada B4P 2R6*

(Received 1 November 2011; published 27 March 2012)

We present an experimental and theoretical investigation of the influence of a uniaxial magnetocrystalline anisotropy on the magnetic textures that are formed in a chiral magnetic system. We show that the epitaxially induced tensile stress in MnSi thin films grown on Si(111) creates an easy-plane uniaxial anisotropy. The magnetoelastic shear stress coefficient is derived from SQUID magnetometry measurements in combination with transmission electron microscopy and x-ray diffraction data. Density functional calculations of the magnetoelastic coefficient support the conclusion that the uniaxial anisotropy originates from the magnetoelastic coupling. Theoretical calculations based on a Dzyaloshinskii model that includes an easy-plane anisotropy predict a variety of modulations to the magnetic order that are not observed in bulk MnSi crystals. Evidence for these states is found in the magnetic hysteresis and polarized neutron reflectometry measurements.

DOI: 10.1103/PhysRevB.85.094429 PACS number(s): 75.25.−j, 75.30.−m, 75.70.Ak

I. INTRODUCTION

Manganese silicide (MnSi) belongs to a group of magnetic noncentrosymmeteric crystals with space group $P2_13$ ($B20$-type structures), called cubic helimagnets.[1,2] In these materials, antisymmetric Dzyaloshinskii-Moriya (DM) interactions induce long-range helical modulations with a fixed sense of the magnetization rotation.[1–3] Recent theoretical work shows that in magnetic materials with intrinsic or induced chirality, DM interactions provide a unique mechanism to stabilize two- and three-dimensional modulations of the magnetic order (*chiral skyrmions*).[4–7] Recently, skyrmionic states have been observed in thin layers of cubic helimagnets[8,9] and in ultrathin magnetic films[10] with surface- or interface-induced DM interactions.[11] Chiral skyrmions have also been observed in thin layers of MnSi.[12] Similar skyrmionic states are predicted to exist in other classes of noncentrosymmetric materials, e.g., in chiral liquid crystals, ferroelectrics, multiferroics, and in confined systems (e.g., nanolayers of magnetic metals)[6,13,14] and are expected to find applications in emerging spintronic technologies.[10,15]

MnSi is an interesting and convenient material to investigate chiral magnetism as well as to explore this class of materials in spintronic devices. In bulk MnSi at zero magnetic field, the competition between the DM and the direct exchange interactions produces helical magnetic order below a Curie temperature of $T_C = 29.5$ K with a wavelength of $2\pi/Q = 18$ nm. The pitch vector $\mathbf{Q}$ points along $\langle 111\rangle$ and the magnetic moments lie perpendicular to it.[16] If an external magnetic field is applied in a direction other than $\langle 111\rangle$, $\mathbf{Q}$ will rotate in the direction of the magnetic field and become parallel to it at a field $\mu_0 H_{C1} \simeq 0.1$ T, as shown theoretically by Plumer and Walker,[17] and confirmed more recently with small-angle neutron scattering (SANS).[18] Above H_{C1}, the magnetic moments form a conical phase, which collapses into a ferromagnetic state at $\mu_0 H_{C2} = 0.6$ T. In cubic helimagnets, there is a narrow temperature interval between the paramagnetic phase and the region of *regular* chiral modulations where a number of complex multidimensional states and numerous physical anomalies have been observed.[19–27] These unconventional textures (so-called precursor states) arise near the T_C as a result of a softening of the magnetization.[13,28] They are characterized by a strong coupling between angular and longitudinal modulations and differ fundamentally from regular chiral phases with angular modulations and a magnetization with a fixed magnitude.[13,26–28] In this paper, we limit our investigation of MnSi thin films to the region of regular modulations, below this precursor regime.

According to theoretical analysis, magnetic modulations in the form of helices, distorted by an applied magnetic field transverse to their propagation direction, here called *helicoids*, and two-dimensional modulations, *skyrmion lattices*, also arise in cubic helimagnets as regular solutions of the corresponding micromagnetic equations.[1,6,29] In bulk samples, they usually only exist as metastable states, while the cone phase corresponds to the global energy minimum over practically the whole region where chiral modulations occur (for details, see Ref. 29). However, the cone phase can be suppressed by intrinsic cubic anisotropies or (more effectively) by induced uniaxial distortions.[29] Thus, a surface-induced uniaxial anisotropy that has an easy axis can stabilize hexagonal skyrmion lattices in magnetic nanostructures with the skyrmion axis along the anisotropy axis. This effect explains the experimental observations of skyrmion lattices in thin layers of cubic helimagnets (Fe,Co)Si and FeGe, as reported in Refs. 8 and 9. An important issue to address, from both a fundamental and an applications point of view, is the response of the helical order in thin films to both surface-induced magnetic couplings and to an external magnetic field. One of the important differences between the results conducted on bulk MnSi and those conducted on thin films is the presence of strain, which is expected to produce a uniaxial anisotropy through magnetoelastic coupling. Generally, both strain and

surface effects offer control of the magnetic anisotropies over a wide range of energies, which should influence the chiral magnetic textures in thin layers of cubic helimagnets.

In contrast to bulk crystals, there has been relatively little work on the magnetic properties of MnSi thin films.[30–33] We have shown that the helical magnetic order is preserved in MnSi(111) films grown on Si(111), which makes this material attractive for spintronics studies of helical magnets. We calculate the magnetic phase diagram for the phenomenological Dzyaloshinskii model[1] with *easy-plane* uniaxial anisotropy in applied magnetic fields transverse to the axis in order to predict the stable modulations of the magnetic order that can be observed in the chiral magnetic thin films. These calculations display existence regions for stable helicoids and skyrmion lattices with tubular skyrmion strings running along the applied field in a direction *perpendicular* to the anisotropy axis.

In this paper, we show that it is possible to induce an easy-plane-type magnetic anisotropy in epitaxial MnSi(111) thin films with a positive and isotropic in-plane strain. Although Si has a lattice constant of 0.5431 nm that is 16% larger than that of MnSi, $a = 0.4558$ nm, the Si(111) surface unit cell is only 3.1% larger than that of MnSi(111) for an epitaxial relationship of $[1\bar{1}0]$MnSi $\|[11\bar{2}]$Si. The noncentrosymmetric MnSi crystal structure results in inversion domains in films grown on Si(111) (Ref. 30) that result in both left- and right-handed helical magnetic domains,[31] which explains the glassy magnetic behavior observed in these films. Polarized neutron reflectometry (PNR) and superconducting quantum interference device magnetometry (SQUID) results show that the pitch vector is along the film normal, and that the helical wavelength $2\pi/Q = 13.9 \pm 0.1$ nm is smaller than measured in bulk material.[31] Here, we present a study of the response of MnSi thin films to a magnetic field that is transverse to $\mathbf{Q}$ displaying interesting reorientation of the helical magnetic order, which is significantly different than in bulk crystals. SQUID magnetometry studies of the magnetic reorientation are complemented by PNR measurements to obtain a depth profile of the magnetization in the films. To understand the origin of these differences, we measure the uniaxial magnetocrystalline anisotropy in the films as a function of thickness by SQUID magnetometry. A comparison of the anisotropy with the strain determined by x-ray diffraction and transmission electron microscopy (TEM) gives the magnetoelastic coupling coefficients. These results are compared to a fully relativistic electron-structure calculation using density functional theory (DFT) of magnetocrystalline anisotropy in rhombohedrally distorted MnSi bulk.

II. MAGNETIC PHASE DIAGRAM OF CHIRAL CUBIC HELIMAGNETS WITH INDUCED UNIAXIAL ANISOTROPY

To model the magnetic states in epitaxial MnSi films, we add an additional uniaxial magnetic anisotropy to the phenomenological free energy for a noncentrosymmetric cubic ferromagnet, which is appropriate as long as the films are strained homogeneously and are not too thin, so that specific surface-induced effects can be neglected. This phenomenological model can be written as a functional $W = \int w(\mathbf{M})dV$ with the energy density w written in terms of a slowly varying magnetization $\mathbf{M}(\mathbf{r})$ and its gradients[1,2]

$$w(\mathbf{M}) = \frac{c}{2}M_s^2(\nabla\mathbf{m})^2 + bM_s^2\mathbf{m}\cdot(\nabla\times\mathbf{m}) + K_u(\mathbf{m}\cdot\hat{\mathbf{n}})^2 - \mu_0\mathbf{H}\cdot\mathbf{M} - \frac{1}{2}\mu_0\mathbf{H}_d\cdot\mathbf{M}, \quad (1)$$

where $\mathbf{m} = \mathbf{M}/M_s$ is a unit vector along the direction of the magnetization $\mathbf{M}$ ($M_s = |\mathbf{M}|$). The magnetic stiffness associated with the exchange interaction c is related to the spin-wave stiffness A by $c = AS/(M_s^2a^3)$, where $S = 0.8$ is the spin per unit cell in units of $\hbar$ and $a = 0.4558$ nm is the lattice constant. The Dzyaloshinskii-Moriya constant D is related to the b coefficient describing the Lifshitz invariant through $b = DS/(M_s^2a^3)$. Aside from these two major exchange couplings that are present in isotropic or cubic chiral magnets,[1] this *Dzyaloshinskii model* only considers Zeeman energy ($\mathbf{H}$ is the applied magnetic field) and demagnetization energy with stray field $\mathbf{H}_d$.[34]

The cubic anisotropy and the anisotropic exchange are omitted in functional (1) because these terms are small. Adding these terms recovers the model used by Bak and Jensen to explain the magnetic structure and magnetization processes in bulk MnSi and related chiral cubic helimagnets.[2] Enhanced uniaxial anisotropy can arise in magnetic nanolayers as a result of elastic strains induced by a lattice mismatch between the magnetic layer and the overlying or underlying layers.[35,36] In addition, anisotropies may be introduced by symmetry breaking at the layers boundaries, and due to physical and chemical modifications at the surfaces and interfaces.[37,38] Depending on material and geometrical parameters, the surface-induced anisotropy can vary from cases when it is strictly confined to the surfaces or interfaces to cases when it smoothly extends into the depth of magnetic layers.[39] An inhomogeneous distribution of the induced anisotropy across the thickness of the film may stabilize specific spatially inhomogeneous magnetic states, so-called *twisted phases*.[39,40] However, their existence regions are restricted to specific relations between material and external parameters.[39,40] In this paper, we neglect effects imposed by spatial inhomogeneity of the induced anisotropy and describe the induced uniaxial anisotropy by an energy contribution with constant K_u [Eq. (1)]. We show in this paper that the MnSi films have an induced anisotropy that is of easy-plane type. For this case, $K_u > 0$ in functional (1), and the ground state of the system is a single harmonic helix with a wave number $Q = b/c$ that propagates along $\hat{\mathbf{n}}$. An applied magnetic field perpendicular to the film surface transforms the helix into the *conical* phase [Fig. 1(a)] with analytical solutions

$$\psi(\xi) = \xi/L_D, \quad \cos(\theta) = H/H_{C2}^{\perp}, \quad (2)$$

where θ is the polar angle of the magnetization with respect to $\hat{\mathbf{n}}$ and ψ is the azimuthal angle, ξ is a spatial variable along the propagation direction, and $L_D = 2\pi c/b = 2\pi/Q$ is the wavelength of the modulation. The out-of-plane saturation field $H_{C2}^{\perp}$ can be expressed as

$$\mu_0 H_{C2}^{\perp} = \frac{2K_0}{M_s} + \frac{2K_u}{M_s} + \mu_0 M_s, \qquad K_0 = \frac{b^2M_s^2}{2c} = \frac{1}{2}\frac{AQ^2}{g\mu_B}M_s, \quad (3)$$

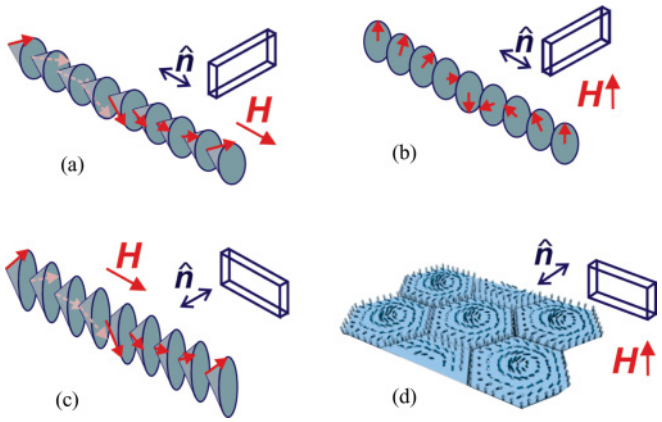

FIG. 1. (Color online) Modulated states in a thin layer of a cubic helimagnet with in-plane magnetization: (a) a *conical* phase that arises in the applied field perpendicular to the film surface, (b) a *helicoid* phase, which is a helix distorted by the applied field perpendicular to the propagation direction, (c) elliptically *distorted conical phases* formed in a strong in-plane magnetic field, and (d) a *hexagonal skyrmion lattice* with elliptical distortions imposed by a uniaxial anisotropy. The unit vector $\hat{\mathbf{n}}$ indicates the direction of the uniaxial anisotropy.

where K_0 is the "effective stiffness" of the conical phase. The conical phase is characterized by the constant modulation period L_D and a linear magnetization curve. Transversally distorted helices (*helicoids*) [Fig. 1(b)] gradually increase their periods with increasing magnetic fields. At a certain critical field $\mu_0 H_h = \pi^2 K_0/(16 M_s)$, helicoids transform into a set of isolated 360° domain walls separating domains with the magnetization along the applied field direction.[1]

One-dimensional modulations propagating along the in-plane field also arise as regular solutions for the model presented in Eq. (1). In such modulations, the uniaxial anisotropy causes elliptical distortions of the "cones" [Fig. 1(c)]. The equilibrium parameters for these *distorted cones* have no analytical solutions. However, for $K_u \ll K_0$ and H near the in-plane saturation field $H_{C2}^{\parallel}$, we can use Eqs. (2) to derive the following result:

$$\mu_0 H_{C2}^{\parallel} = (2K_0 - K_u - K_m)\, M_s^{-1},$$
$$K_m = \mu_0 M_s^2 \frac{L_D}{4\pi d}\left[1 - \exp\left(-2\pi d/L_D\right)\right], \qquad (4)$$

where $K_m(d/L_D)$ is the stray field contribution and d is the film thickness.

The equations that minimize the energy functional (1) with an in-plane magnetic field also include solutions for two-dimensional modulations in the form of *hexagonal skyrmion lattices* with elliptical distortions caused by the uniaxial anisotropy [Fig. 1(d)]. We have studied the magnetic phase diagram that results from model (1) for a bulk system with periodic boundary conditions by using numerical methods, as in previous work.[6,13] We have calculated stable solutions rigorously of one- and two-dimensional modulated states for $\mathbf{H} \perp \hat{\mathbf{n}}$ by direct energy minimization and testing their stability. By comparing the energies of these solutions, we determine the thermodynamically stable states and the first-order transition lines between them. The resulting magnetic

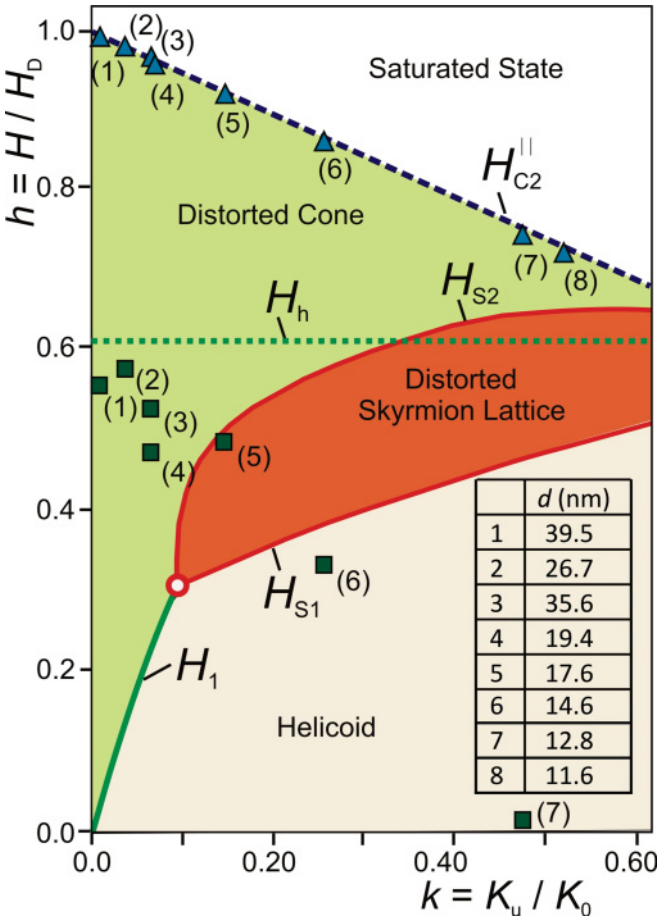

FIG. 2. (Color online) Low anisotropy range of the magnetic phase diagram in reduced variables for uniaxial anisotropy $k = K_u/K_0$ and applied magnetic field $h = H/H_D$ for model (1) with an in-plane magnetic field [$H_D = 2K_0/M_s$ is the saturation field for a bulk cubic helimagnet with $K_u = 0$ and K_0 is an "effective stiffness" (Eq. (3))]. The regions of global stability for helical and skyrmionic states are indicated by different colors. Solid lines designate the first-order transitions: H_1 represents the transition between helicoid and distorted cone, and H_{S1} and H_{S2} are transitions from a distorted skyrmion lattice to helicoid and distorted cones, respectively. The dashed line indicates the critical field $H_{C2}^{||}$ [Eq. (4)] for the distorted cone phase. $H_h = \pi^2 K_0/(16\mu_0 M_s) = 0.617 H_D$ is the transition between the helicoid and the saturated states. Triangles and squares show experimental values of critical fields $H_{C2}^{||}$ and H_α for MnSi films of different thickness d.

phase diagram (Fig. 2) demonstrates that $\mathbf{H} \perp \hat{\mathbf{n}}$ can induce skyrmion phases in noncentrosymmetric magnets with an easy-plane-type uniaxial anisotropy when K_u is above a threshold value. However, the helicoids propagating along the axis of the uniaxial anisotropy retain thermodynamical stability over a wide range of magnetic fields and transform by a first-order process, either into the distorted conical phase at a critical field $H_1(K_u/K_0)$ (for $K_u < K_u^* = 0.12K_0$) or into the skyrmion lattice. In the magnetic phase diagram (Fig. 2), critical lines $H_{S1}(K_u/K_0)$ and $H_{S2}(K_u/K_0)$ separate the skyrmionic states from the regions with one-dimensional modulations.

The results of the model apply to the strained MnSi films investigated in this work. However, the neglected effects of

cubic anisotropy and additional surface-induced anisotropies can modify the details and quantitative evaluation of the magnetic phase diagram. For thin films in particular, the isotropy of the chiral Dzyaloshinskii model could be impaired and inhomogeneous competing surface anisotropies, e.g., with easy-axis character, may become important.

III. MAGNETIC CHARACTERIZATION

We performed SQUID measurements of MnSi(111) thin films in order to determine the energy scales that govern the spin reorientation transition. The films were grown on Si(111) by molecular beam epitaxy (MBE), and capped with a protective 20-nm-thick amorphous Si cap, as described in Ref. 31. The M-H loops were measured in an applied magnetic field oriented along the out-of-plane [111] and the in-plane [$1\bar{1}0$] directions at a temperature of $T = 5$ K. The linear diamagnetic susceptibility of the substrate was determined from the least-squares fits to M between $\mu_0 H = 3$ and 5 T and subtracted from the data. Six representative curves are shown in Fig. 3. The out-of-plane curves are qualitatively similar to bulk for all film thicknesses.[41] M increases approximately linearly with field up to a field $H_{C2}^{\perp}$, and reaches a saturation magnetization $M_s = 163 \pm 3$ kA/m, which corresponds to a moment $\mu = 0.416 \pm 0.003$ μ_B/Mn as compared to 0.39 μ_B/Mn in bulk. The knee in the M-H loops, which is determined from the minimum in d^2M/dH^2, is used as a measure of $H_{C2}^{\perp}$ and is plotted as a function of thickness in Fig. 4.

For in-plane magnetic fields, the shape of the M-H loops is qualitatively different than bulk. The first difference is the existence of a remanent magnetization. Since the magnetization lies in plane with the pitch vector along the film normal, there are uncompensated moments when the film thickness is a noninteger multiple of the helical wavelength. Oscillations in the remanent magnetization as a function of film thickness provide a measure of this wavelength.[31] Second, we find first-order-like jumps in the magnetization in Figs. 3(b) and 3(c), labeled H_α. For some thicknesses, there is an additional kink in the magnetization below H_α, which is labeled H_β in Fig. 3(c). The values for the in-plane saturation fields $H_{C2}^{\parallel}$ were determined in the same way as for $H_{C2}^{\perp}$, with the exception of the two lowest film thicknesses where rounding of the M-H curves prevented a clear determination of the minimum in the second derivative. In these two cases, the knee was determined by extrapolation of the low-field M values of the M-H curve up to M_s, and the second derivates were calculated from the decreasing-H branch of the hysteresis loops since they provided sharper transitions.

The effective stiffness of the conical phase can be derived from the measured saturation fields $H_{C2}^{\perp}$ and $H_{C2}^{\parallel}$:

$$K_0 = \frac{M_s}{6}\left(\mu_0 H_{C2}^{\perp} + 2\mu_0 H_{C2}^{\parallel} - \mu_0 M_s + \frac{2K_m}{M_s}\right). \quad (5)$$

Since we have found that the helical wavelength $2\pi/Q = 13.9 \pm 0.1$ nm is independent of d for a film thickness range of at least 7 to 40 nm,[31] K_0 provides a measure of the spin-wave stiffness. Figure 5(b) shows that A is approximately independent of thickness with a mean value

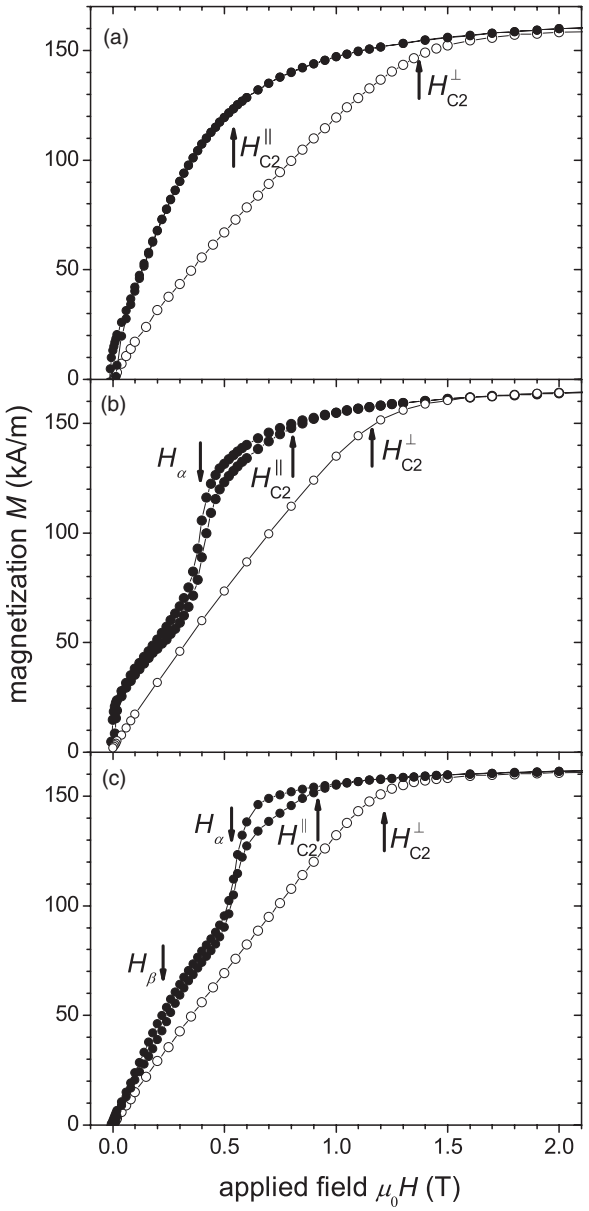

FIG. 3. SQUID M-H curves of MnSi thin films with an in-plane field applied along [$1\bar{1}0$] (filled points) and out-of-plane field along [111] (open points) measured at $T = 5$ K. The film thicknesses are $d = 11.6$ nm (a), 17.6 nm (b), and 26.7 nm (c).

$A = 0.45 \pm 0.01$ meV nm^2 as compared to the bulk value $A \simeq 0.50$ meV nm^2.[42,43] This is consistent with the fact that T_C is nearly constant between $d = 10$ and 40 nm. Given that $Q = D/A$, we then infer that $D = 0.203 \pm 0.005$ meV nm is larger than the bulk value, 0.18 meV nm. However, Grigoriev *et al.* argue that the Dzyaloshinskii interaction is best characterized by $D/(\mu a)$ since they find it to vary about a value of 1.15 ± 0.01 meV/μ_B for both the $Mn_{1-x}Fe_xSi$ and $Fe_xCo_{1-x}Si$ B20 alloys.[44,45] We obtain a value $D/(\mu a) = 1.06 \pm 0.03$ for the films that is in good agreement with this value. The 22% reduction in the wavelength of the helix in the thin films can therefore be understood by the combination of a decrease in the spin-wave stiffness, and the increase in D due to the increase in the magnetic moment of the film.

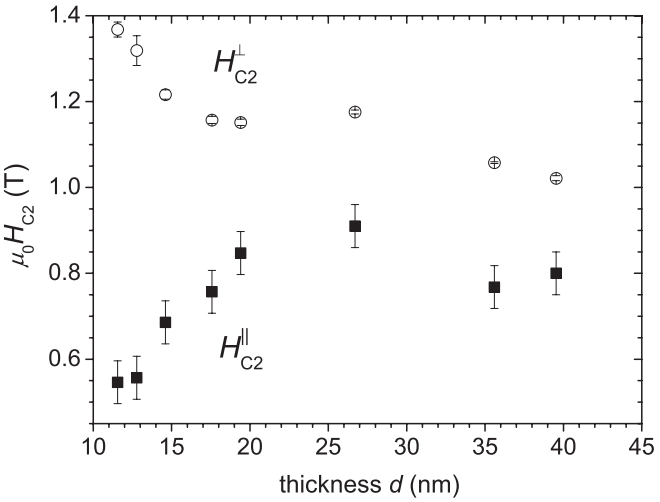

FIG. 4. The in-plane saturation field (filled squares) and the out-of-plane saturation field (open circles) determined from M-H curves measured at $T = 5$ K, like those shown in Fig. 3

The magnetocrystalline anisotropy, which is the second energy scale important to understand the magnetic phase diagram, is also determined from the saturation fields $H_{C2}^{\perp}$ and $H_{C2}^{\parallel}$,

$$K_u = \frac{M_s}{3}\left(\mu_0 H_{C2}^{\perp} - \mu_0 H_{C2}^{\parallel} - \mu_0 M_s - \frac{K_m}{M_s}\right), \qquad (6)$$

and is plotted in Fig. 5(a). The anisotropy is found to be positive, which shows that it is of easy-plane type.

Given the epitaxially induced strain in the films, this uniaxial anisotropy would be expected to originate, at least in part, from magnetoelastic coupling. Furthermore a surface

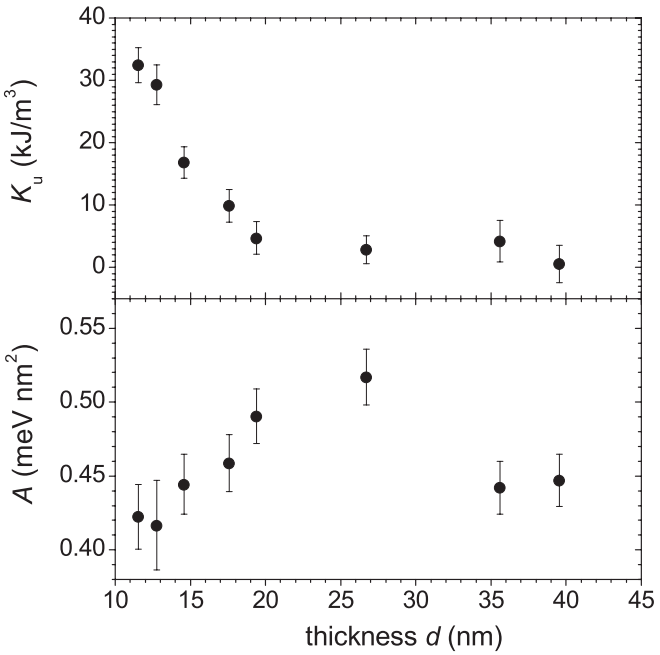

FIG. 5. The uniaxial magnetocrystalline anisotropy (a) and the exchange stiffness (b), calculated from the $H_{C2}^{\perp}$ and $H_{C2}^{\parallel}$ in Fig. 4, as a function of MnSi film thickness

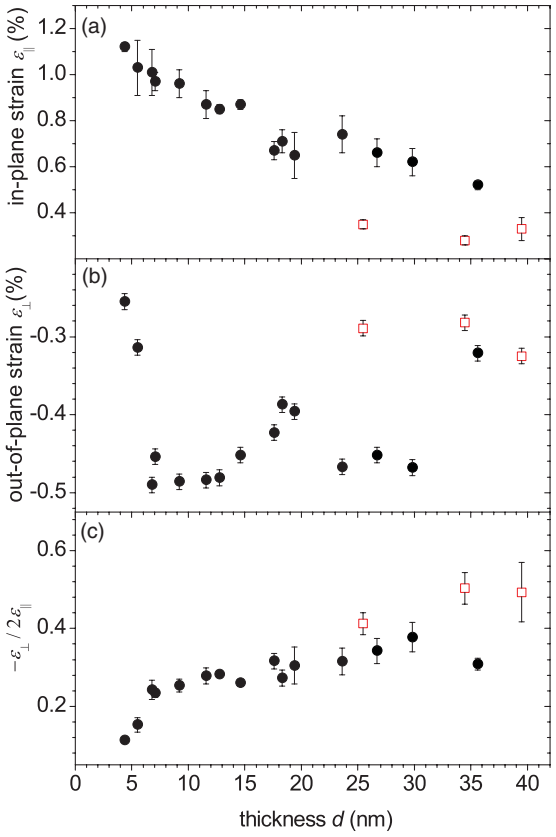

FIG. 6. (Color online) (a) In-plane elastic strain measured from plane-view TEM selected area diffraction patterns. (b) Out-of-plane strain determined from x-ray diffraction measurements of the MnSi(111) peak. In both sets of measurements, the Si substrate was used as an internal calibration standard. (c) Ratio of the out-of-plane strain to twice the in-plane strain. The three samples indicated by open red squares contain $MnSi_{1.7}$ precipitates in excess of 20%. All error bars are $\pm 1\sigma$.

anisotropy of the form K_u^s/d cannot fit the data in Fig. 5(a). From the magnetoelastic free energy, expressed in terms of the components of the directional cosines m_i and the strains ϵ_{ij}, defined with respect to the cubic axes of MnSi,[46]

$$w_{me} = B_1\left(\epsilon_{xx}m_x^2 + \epsilon_{yy}m_y^2 + \epsilon_{zz}m_z^2\right) + B_2(\epsilon_{xy}m_x m_y + \epsilon_{yz}m_y m_z + \epsilon_{xz}m_x m_z), \qquad (7)$$

one can show that a trigonal distortion of the (111) planes produces an isotropic magnetoelastic stress energy contribution B_1. However, the magnetoelastic shear stress contribution to the free energy of the film is anisotropic:

$$w_{me} = \tfrac{1}{2}B_{2,\mathrm{eff}}(\epsilon_{\perp} - \epsilon_{\parallel})(\mathbf{m}\cdot\hat{\mathbf{n}})^2. \qquad (8)$$

If we attribute the uniaxial magnetocrystalline anisotropy to this contribution, we can obtain an estimate of an effective magnetoelastic shear stress $B_{2,\mathrm{eff}}$. To this end, we measured the in-plane strain $\epsilon_{\parallel}$ from TEM selected area diffraction patterns and the out-of-plane strain $\epsilon_{\perp}$ by using x-ray diffraction curves from the MnSi(111) planes, both of which were performed at room temperature. The results are shown in Fig. 6. The strains are higher in the MBE samples compared to the solid-phase epitaxy (SPE) samples.[30] We attribute the higher residual

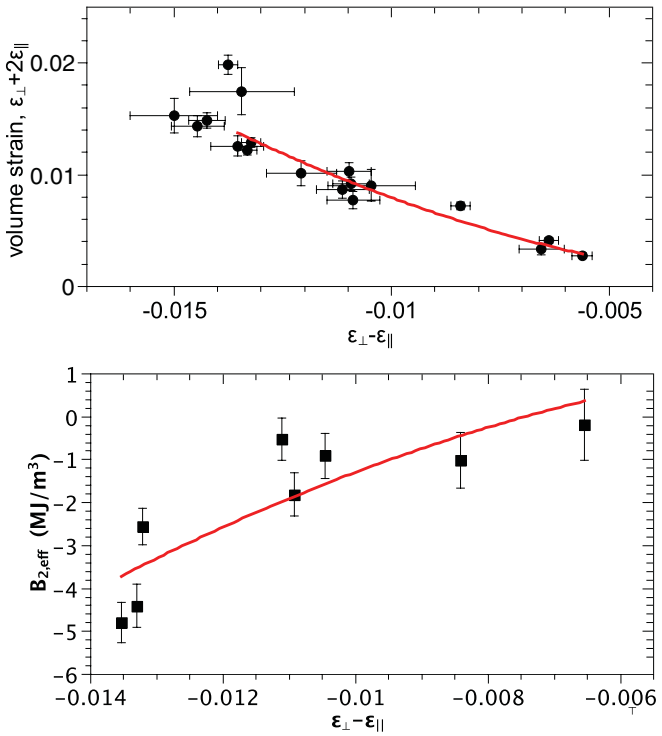

FIG. 7. (Color online) (a) The volume strain as a function of three times the shear strain. The red line shows the polynomial fit to the data over the range cover by the $B_{2,\mathrm{eff}}$ data. (b) The effective magnetoelastic shear stress, where the red line is a fit to the data. The fit in (a) and (b) gives $B_2 = 1.6 \pm 1.0$ MJ/m^3, $D_1 = -78 \pm 20$ MJ/m^3, and $D_2 = -460 \pm 120$ MJ/m^3. All error bars represent $\pm 1\sigma$.

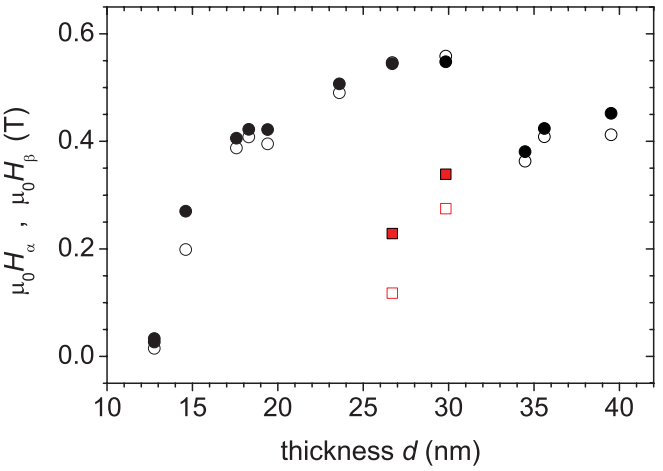

FIG. 8. (Color online) The in-plane fields H_α and H_β, as shown in Fig. 3, determined from the peak in dM/dH of the SQUID measurements with the magnetic field along [1$\bar{1}$0]. The filled (open) circles show H_α calculated from the decreasing-H (increasing-H) branch of the M-H curve measured at $T = 5$ K. The red squares show H_β for decreasing H (filled squares) and increasing H (open squares).

strains in the films to the shorter annealing times during MBE growth. On the other hand, the ratio $\epsilon_\perp/2\epsilon_\parallel$, which is related to the ratio of the bulk modulus to the shear modulus c_{44},[30] is the same for both MBE and SPE grown samples, which implies that the elastic constants for both sets of samples are the same, despite the presence of a small concentration of $MnSi_{1.7}$ precipitates in MBE grown samples. A large concentration of precipitates, however, does affect the elastic properties of the films. The strain in three of the samples that contained more than 20% $MnSi_{1.7}$, as determined from plane-view TEM images, has relaxed more than the other samples. The $\epsilon_\perp/2\epsilon_\parallel$ is high in these samples, which suggests the precipitates do soften the c_{44} of the films when in large concentrations. Despite these differences, the magnetic moments of the MnSi films remain unaffected by the presence of the $MnSi_{1.7}$.

We made estimates of the effective magnetoelastic shear stress $B_{2,\mathrm{eff}}(\epsilon) = 2K_u/(\epsilon_\perp - \epsilon_\parallel)$, shown in Fig. 7(b). Here, we assume that the magnetocrystalline surface anisotropy is negligible. This is a reasonable assumption since the surface anisotropies K_u^s are in the range $(0.2 - 1)$ mJ/m^2 for Fe, Co, and Ni,[35,37,47] and would be expected to be considerably smaller for MnSi given the small $M_s = 163$ kA/m and that K_u scales as M^2.[48–50]

The magnetoelastic shear stress was found to vary with thickness, as found for other thin-film systems. Wedler *et al.* measured the nonlinear $B_{2,\mathrm{eff}}$ in Fe/MgO(100), and introduced an $\epsilon_\parallel$-dependent contribution to $B_{2,\mathrm{eff}}$.[51] However, as pointed out in Ref. 52, this *ansatz* does not properly account for the symmetry of the crystal. In the case of a trigonal distortion of a MnSi(111) film, nonlinear magnetoelastic theory[53] gives a contribution proportional to the shear strain, with coefficient D_1, as well as to the volume strain, parametrized by D_2:

$$B_{2,\mathrm{eff}} = B_2 + D_1(\epsilon_\perp - \epsilon_\parallel) + D_2(\epsilon_\perp + 2\epsilon_\parallel), \qquad (9)$$

where B_2 is the linear magnetoelastic shear stress. Since the volume and shear strains are related through the elastic constants, we fit the volume strain in Fig. 7(a) to $c_1(\epsilon_\perp - \epsilon_\parallel) + c_2(\epsilon_\perp - \epsilon_\parallel)^2$ over a range spanned by the data in Fig. 7(b) to enable a fit to the $B_{2,\mathrm{eff}}$ with a single variable. The parameters c_1 and c_2 together with the fit in Fig. 7(b) give $B_2 = 1.6 \pm 1.0$ MJ/m^3, $D_1 = -78 \pm 20$ MJ/m^3, and $D_2 = -460 \pm 120$ MJ/m^3.

To date, there are no values for B_2 for MnSi provided in the literature. However, the magnetoelastic stress B_1 equals $2B_2$ in an isotropic medium.[54] By analysis of the magnetostriction data given in Ref. 55, and by correcting the scale in the plot of the low-field magnetostriction data, as pointed out in Ref. 56, we obtain $B_1 \simeq 1$ MJ/m^3 for bulk MnSi at low temperature. Therefore, $B_2 = 1.6$ may overestimate the magnetoelastic shear stress in the films. However, the reasonable fit shows that the uniaxial anisotropy can be explained in terms of a magnetoelastic effect.

The measurement of the uniaxial anisotropy provides a basis for attempting to understand the reorientation transition in MnSi thin films. Unlike the out-of-plane measurements, the M-H curves measured with an in-plane magnetic field show significant departures from the characteristic behavior of bulk MnSi, as described by the in-plane transition fields H_α and H_β shown in Fig. 3. We plot the values for these fields obtained from peaks in dM/dH (see Fig. 8). The first-order-like step at H_α only appears above a thickness $d = 12$ nm, which is close in magnitude to $2\pi/Q$. For film thicknesses close in value to $4\pi/Q$, a second transition H_β appears. These two transitions are more difficult to explain with existing models. Plumer

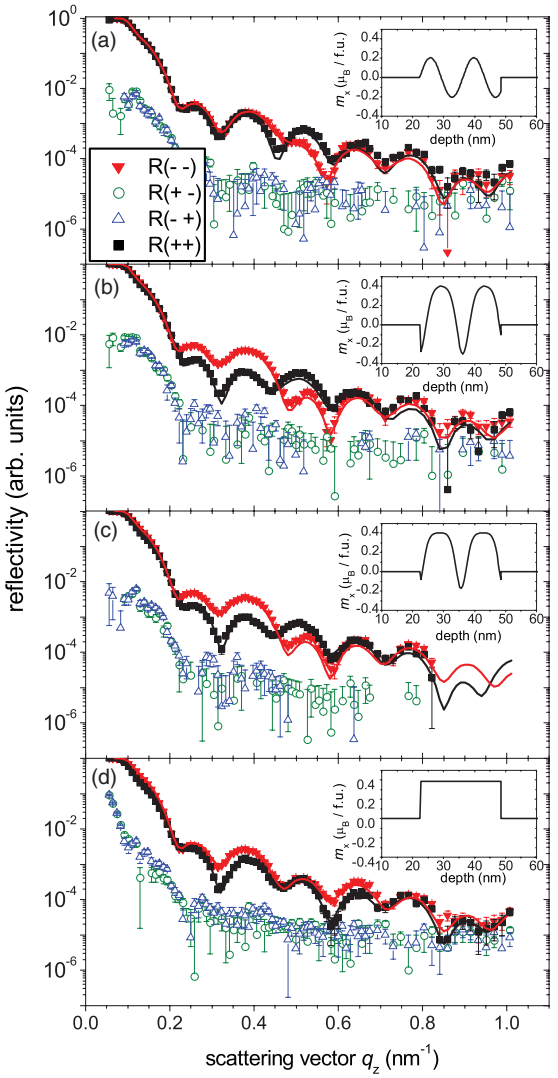

FIG. 9. (Color online) PNR with $\pm 1\sigma$ error bars of 20 nm Si/26.7 nm MnSi/Si(111) measured at $T = 6$ K. The magnetic field applied along the in-plane $[1\bar{1}0]$ direction is (a) 1 mT, (b) 0.3 T, (c) 0.5 T, and (d) 0.8 T. The fits to the PNR data, shown by the solid lines, yield the magnetic moment profiles given in each of the insets.

and Walker modeled the reorientation of the helical order in bulk MnSi where small departures from linear M-H curves are observed below the reorientation transition $H_{C1} \simeq 0.1$ T.[17] However, their solutions to a Landau-type free energy are not able to account for the large values of H_α relative the $H_{C2}^{\perp}$.

IV. MAGNETIC DEPTH PROFILES

In order to better understand the magnetic structure during reorientation, we performed a series of PNR measurements on a $d = 26.7$-nm-thick film with the aim of determining a depth profile of the magnetization for a range of applied magnetic fields. The results of the measurements performed on the NG-1 reflectometer at the NIST Center for Neutron research are shown in Fig. 9. We present measurements with the magnetic field and neutron polarization along the in-plane $[1\bar{1}0]$ direction in Fig. 9, in contrast to our previous measurements where an out-of-plane orientation enabled a

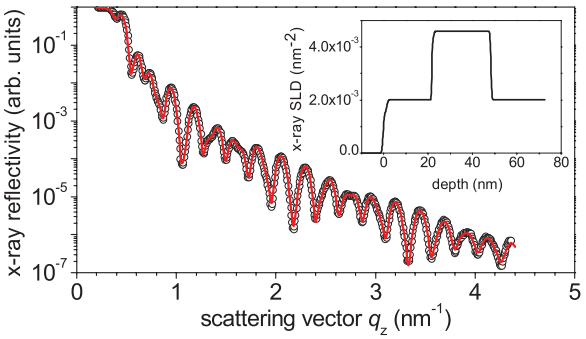

FIG. 10. (Color online) XRR measurements of the 20 nm Si/26.7 nm MnSi/Si(111) sample shown in Fig. 9. The solid line is a fit to the data, which gives the x-ray SLD shown in the inset.

direct measure of the pitch of the helix.[31] Samples were field cooled with $\mu_0 H = 0.8$ T applied along the $[1\bar{1}0]$ direction to a temperature of 6 K, and then four sets of measurements were performed in fields of 1 mT, 0.3 T, 0.5 T, 0.6 T, and 0.8 T. In this more conventional geometry, the scattering cross sections $R(++)$ and $R(--)$ are sensitive to both chemical and magnetic structure. Evidence for helical order would normally appear as a Bragg-type peak in the $R(+-)$ or $R(-+)$ channels, which are sensitive to the in-plane component of the magnetization that is perpendicular to the field direction. However, the presence of left- and right-handed magnetic domains largely cancel one another, evidenced by the small spin-flip (SF) signal, as can be seen in Fig. 9.

In order to extract the magnetic scattering length, we infer the nuclear scattering length density (SLD) profile from the x-ray SLD profile determined from a fit to the x-ray reflectometry (XRR) data in Fig. 10. The x-ray SLD is uniform across the thickness of the silicide film and agrees well with the value expected for MnSi, which indicates that the film is single phase without any secondary phase, in agreement with TEM measurements. We use the nuclear SLD to then fit $R(++)$ and $R(--)$ in Fig. 9 and obtain the magnetic SLD profile displayed in each of the insets. A uniform magnetic SLD profile that corresponds to a moment of $m = 0.38\mu_B$/Mn fits the 0.8-T data well. A conical phase with $\mathbf{Q}||[1\bar{1}0]$ is consistent with such an SLD profile since the component of the magnetization in the field direction in this orientation is constant throughout the film. The cone angle inferred from PNR measurements, $\theta = \cos^{-1}(m/m_{\rm sat}) = 25^\circ$, is in reasonable agreement with $\theta = \cos^{-1}(H/H_{C2}^{\parallel}) = 28^\circ$ obtained from SQUID measurements.

In an applied field of 1 mT oriented in the in-plane $[1\bar{1}0]$ direction, the pitch vector $\mathbf{Q}$ is pointing in the out-of-plane [111] direction. A sinusoidal magnetic SLD profile with a period of $2\pi/Q = 13.9 \pm 0.01$ nm provides a good fit to the data. This is entirely consistent with the out-of-plane measurements.[31] The small magnetic moment of 0.20 μ_B/Mn that is obtained from the fit is accounted for by the presence of domains. The SLD profile for the 0.3 T field in Fig. 9(b) shows distortions to the sinusoidal SLD, which become greater at 0.5 T. The evolution and reorientation of the helical order, however, shows clear departures from bulk behavior. The PNR data provide an in-plane average of the component of the magnetization in the direction of the magnetic field. The fact that the depth dependence of the magnetization is described

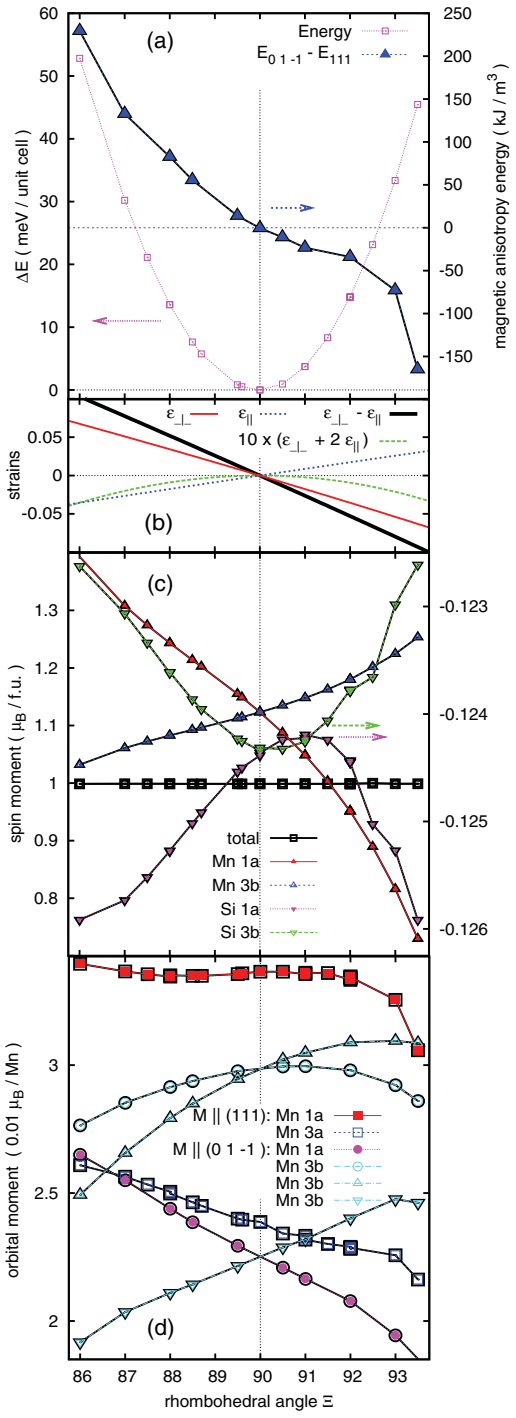

FIG. 11. (Color online) Results from density functional theory calculations for strained MnSi: (a) the dependence of the energy increase ΔE on the rhombohedral angle Ξ with fixed lattice constant $a = 0.4556$ nm and the calculated anisotropy for the magnetization along the rhombohedral axis, parallel to [111], and perpendicular to the axis along $[1\bar{1}0]$. (b) Dependence of strain components on Ξ for the deformation with constant lattice parameter. Note the factor 10 for the volume strain $\epsilon_\perp + 2\epsilon_\parallel$. (c) Corresponding evolution of spin moments for different sites in the rhombohedral cell. (d) Comparison of orbital magnetic moments on the different Mn sites for the magnetization parallel and perpendicular to the rhombohedral axis. In the latter case, the equivalence of the 3*b* sites is lost and the orbital magnetic moments split.

by the layered model rules out a second-order-like transition where the pitch vector rotates in the direction of the magnetic field. Furthermore, the magnetization can be seen to be larger in the field direction than in the antiparallel direction. This difference contributes to the net magnetization, and is in agreement with $M(H)$ plotted in Fig. 3(c).

V. THEORETICAL CONSIDERATIONS AND DISCUSSION

In the following two sections, the experimental information is discussed using additional insights from theoretical calculations. The first section reports *ab initio* calculations to assess the induced uniaxial anisotropy in strained cubic helimagnets. The results corroborate the basic magnetic model of a chiral magnet with a homogeneous easy-plane uniaxial anisotropy [Eq. (1)] to describe the properties of the epitaxial MnSi films. In the second part, the experimental observations on the field-driven evolution of the modulated states are discussed.

A. Comparison with electronic-structure calculations

In order to ascertain the character and origin of the uniaxial anisotropy in strained epitaxial MnSi films, we have performed electronic-structure calculations. The calculations for rhombohedrally distorted MnSi provide theoretical estimates for the magnetoelastic coupling coefficient B_2 and the induced uniaxial anisotropy, which is a bulk effect present in homogeneously strained films. Density functional theory calculations of the electronic structure are useful to understand and evaluate the properties of *d*-electron-based metallic magnetic systems.[57] In particular, trends in magnetic properties of metallic nanostructures can be understood from such calculations, even though the exact quantitative determination of small spin-orbit effects such as magnetic anisotropies or magnetostriction coefficients still poses severe problems (see Refs. 50, 58 and the references therein). In the present MnSi films, the lattice stretches are sizable so that the induced *uniaxial* anisotropy can be estimated from electronic-structure calculations, although the intrinsic cubic anisotropies in this material that derive from higher-order spin-orbit coupling effects are too small to be calculated reliably by DFT methods. To address the limit of relatively thick films, we neglect the proper surface-induced anisotropies.

The isotropic in-plane strain in the (111)-oriented films transforms the cubic lattice from the structure described by space group $P2_13$ (#198) into a rhombohedrally distorted structure with symmetry $R3$ (#146). We performed calculations using a full-potential local orbital method, as implemented in the FPLO code[59] with the generalized gradient approximation (GGA) parametrized by Perdew, Burke, and Ernzerhof.[60] The variation of total energy with respect to the rhombohedral angle Ξ is evaluated from a full relativistic calculation with the quantization axis (magnetization direction) in various directions.[61] In the calculations, the lattice constant has been kept at a fixed value of $a = 0.4556$ nm, as was determined previously from calculations by optimizing the structure of the cubic cell, including the cell parameters. The calculated results for the cubic MnSi structure are in good agreement with earlier DFT studies.[62] In the rhombohedrally distorted cell, the site positions 4*a* for the Mn and Si in the cubic structure are split

into two crystallographic inequivalent positions $1a$ and $3b$. For each rhombohedral angle $\Xi = \pi/2 - 2(\epsilon_\perp - \epsilon_\parallel)/3$, the lattice cell of the distorted bulk MnSi was first optimized by a scalar relativistic calculation. In these calculations, the site positions of all atoms have been relaxed so that forces on the atom were less than 10^{-3} eV/Å. In these optimized structures, full relativistic calculations are used to estimate the magnetocrystalline anisotropy. The energy was converged to values better than 4×10^{-7} eV/unit cell and the density to better than 10^{-6}. It was checked that the reciprocal space integration with a k-mesh subdivision of $22 \times 22 \times 22$ is sufficient to obtain satisfactory convergency of the fully relativistic total energies. As expected, the method is unable to resolve the anisotropy for different magnetization directions *in the plane*, which was checked by performing calculations with the quantization axis along the $[\bar{1}\bar{1}2]$, $[1\bar{1}0]$, and $[\bar{1}\bar{1}2] + \sqrt{6}[1\bar{1}0]$ directions. Thus, the sixfold basal plane anisotropy in the isotropically strained MnSi(111) should be below a few μeV/f.u. Therefore, we only compare results for the quantization along the crystallographic [111] axis with those with the axis along the in-plane direction $[1\bar{1}0]$ in the following discussion.

Figure 11(a) shows the dependence of the total energy ΔE on Ξ with respect to the minimum energy for the cubic structure $\Xi = 90^\circ$ and the magnetocrystalline anisotropy energy (MAE) evaluated as the difference of the total energies for the two different quantization axes, MAE$= E_{\rm tot}^{111} - E_{\rm tot}^{01-1}$. The figure shows that the isotropic in-plane expansion induces an easy-plane magnetic anisotropy, while compressively strained films would acquire an out-of-plane easy-axis anisotropy. Figure 11(b) shows the dependence of the different strain components on rhombohedral angle Ξ, which are almost linear over the relevant range of angles, while the volume strain $\epsilon_\perp + 2\epsilon_\parallel$ is almost zero for the deformation mode used in the calculations. The magnetoelastic coupling coefficient $B_2^{\rm DFT} = -2.1 \pm 0.2$ MJ/m^3 is calculated from the slope of MAE($\Xi = 90^\circ$). Similarly, the leading nonlinear magnetoelastic coupling coefficient $D_1^{\rm DFT} = -17.9 \pm 1.5$ MJ/m^3 can be estimated from a nonlinear fit. The total magnetic moment remains constant under strain. However, there is a marked redistribution of spin moment between the different Mn and Si sites, as shown in Fig. 11(b). A sizable induced spin moment on Si is found, which undergoes minor changes in the strained lattice. The redistribution of spin moments on Mn is accompanied by a complex dependency of the corresponding orbital magnetic moments on the different Mn sites that also depend on the quantization direction [Fig. 11(c)]. These orbital moments are associated with the magnetic anisotropy energy. The observed dependence indicates an intricate mechanism due to the strain that makes all the MnSi $4a$ sites inequivalent for a magnetization perpendicular to the rhombohedral axis. The calculated orbital moments on Si are very small.

MnSi is described as a weak band ferromagnet subject to strong spin fluctuations, which strongly reduce the static spin polarization in the low-temperature magnetically ordered state.[63] Thus, the experimentally determined magnetic moment that is 0.39 μ_B/Mn in bulk MnSi is enhanced to about $S_{\rm exp} = 0.42\mu_B$/Mn in the epitaxial films with a slight volume expansion. As in previous DFT calculations on MnSi with B20-structure,[62] we find a net spin moment of $S^{\rm DFT} = 1.00\mu_B$/Mn. As a result of the enhanced spin moment in the DFT calculations that neglect quantum-dynamical spin fluctuations, the MAE is also overestimated. In order to provide a more realistic estimate on the uniaxial anisotropy energy E_a from the calculations, we assume that the MAE scales with the magnetization. A renormalization considering spin fluctuations should behave as $E_a =$MAE$\,(S_{\rm exp}/S^{\rm DFT})^n$. The effects of thermal and quantum dynamics at the zero point both cause a reduction of the magnetization, which essentially influences the macroscopic magnetic properties in the same way. Therefore, we can rely on recent results on the *temperature* dependence of the magnetic uniaxial anisotropies in band ferromagnets, which find a scaling of MAE with the magnetization and an exponent $n = 2$.[48–50] Thus, a simple rescaling of the MAE by a factor $(0.42/1.00)^2 = 0.18$ is appropriate to estimate a theoretical magnetoelastic coupling coefficient of bulk MnSi of $B_2 = -0.37$ MJ/m^3 and a nonlinear coefficient of $D_1 = -3.2$ MJ/m^3. In view of the large uncertainties regarding the theoretical treatment of the spin-fluctuation effect, there is still a reasonable agreement of this value with the experimental data shown in Fig. 7.

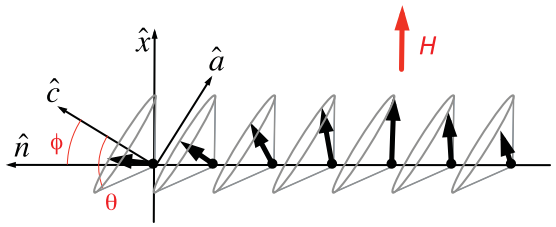

FIG. 12. (Color online) Diagram of a skewed conical phase in an in-plane magnetic field, where $\hat{\mathbf{n}}$ is the film normal and $\hat{\mathbf{x}}$ is the direction of the applied magnetic field H. The wavefronts of this phase remain parallel to the surface, while the axis of the cone $\hat{\mathbf{c}}$ cants in the direction of the field by an angle ϕ.

B. Field-driven modulated structures

The profiles from the PNR in applied magnetic fields (Fig. 9) are unusual. If one assumes a one-dimensional chiral modulated state to explain these profiles, then one is led to consider a skewed conical phase with anharmonic distortions. The lth harmonic of the magnetic moment for such a structure as a function of depth z,

$$\mu_l(z) = \mu_l \cos(\theta)\hat{\mathbf{c}} + \mu_l \sin(\theta)[\cos(l\mathbf{Q}\cdot\hat{\mathbf{n}}z)\hat{\mathbf{a}} + \sin(l\mathbf{Q}\cdot\hat{\mathbf{n}}z)\hat{\mathbf{b}}], \tag{10}$$

is expressed in terms of an orthonormal coordinate system

$$\hat{\mathbf{a}} = \cos(\phi)\hat{\mathbf{x}} - \sin(\phi)\hat{\mathbf{n}}, \quad \hat{\mathbf{b}} = \hat{\mathbf{y}}, \quad \hat{\mathbf{c}} = \sin(\phi)\hat{\mathbf{x}} + \cos(\phi)\hat{\mathbf{n}}. \tag{11}$$

The coordinate axes are written in terms of ϕ, the angle of the cone axis with respect to $\hat{\mathbf{n}}$, and in terms of the unit vectors $\hat{\mathbf{x}}\|[1\bar{1}0]$, $\hat{\mathbf{y}}\|[\bar{1}\bar{1}2]$, and $\hat{\mathbf{n}}\|[111]$, as shown in Fig. 12.

The skewed cone cants in the direction of the field, while the wavefronts of the spin density wave remain perpendicular to $\hat{\mathbf{n}}$, in contrast to a conical phase where the wavefronts are perpendicular to the $\hat{\mathbf{c}}$ direction. For the case of $\mu_0 H = 0.5$ T, a first harmonic $\mu_1 = 0.42\mu_B$/Mn and second harmonic $\mu_2 = 0.12\mu_B$/Mn with $\theta = 56^\circ$ and $\phi = 40^\circ$ are able to accurately reproduce the magnetic SLD profile. Field-induced second harmonics have been observed in bulk MnSi,[43,64] and were also predicted by Plumer and Walker.[65] However, such a skewed conical phase has not been seen previously.

The one-dimensional skewed conical phase rationalizes the experimental observations and is one of the possible structures to explain the unusual magnetization processes. It is clear from an unrestricted search for one-dimensional static magnetic states that skewed conical helices do not exist as solutions in the basic magnetic model with a homogeneous easy-plane uniaxial anisotropy [Eq. (1)]. However, it is equally clear that epitaxial thin films may possess a number of additional interactions stemming from the surfaces, which could eventually stabilize such distorted modulated structures. There is ample choice of possible competing and inhomogeneously distributed anisotropies, e.g., the intrinsic cubic anisotropies, that may cause anharmonicities, and competing easy-axis surface anisotropies. Moreover, in the strained films, the isotropy of the chiral DM interaction may be lost, so that the in-plane and out-of-plane helical modulations become energetically different.

The phase diagram, Fig. 2, enumerates the basic conformations of the possible magnetic modulations in an almost isotropic chiral magnet with an easy-plane anisotropy: the flat helicoidal structure in the field plane, the conical helices, and skyrmion lattices. It also shows that there is a close competition between these states around a triple point, where these three structures can coexist. All transformations between these states are expected to be first-order processes. Moreover, this indicates the possibility of severe history dependence and hysteresis in the magnetization processes. Weaker interactions, e.g., intrinsic cubic anisotropies[2] and additional surface effects, are not considered in the phase diagram. These couplings could lead to modifications or distortions of the basic modulated structures. Quantitative agreement with experiment is expected for the saturation of the conical phase at field H_{C2} because this transition is continuous and starts out from the unique saturated state. This field is used to determine the induced anisotropy K_u of the films in Fig. 2. For all other transition lines and transformation processes between these different states, a quantitative agreement is not to be expected as their energies are very close and relative thermodynamical stability may be shifted by minor additional effects.

The thicker films that show a lower easy-plane anisotropy display a hysteretic transformation process at the characteristic field H_α, which is just below the field H_h, for transformations from flat helicoids into the saturated state. It is important to understand the peculiar nature of this transformation, which does not destroy the helical kinks (360° rotations) of the magnetization in an infinite system. Rather, the transformation retains the localized core of these kinks while their tails are stretched to infinity, so that the period of the helicoid diverges. The reverse transformation requires the nucleation of single kinks, which then assemble into a periodic one-dimensional lattice at the *nucleation transition* H_h. This means that the helicoid and the competing conical state, propagating transverse to it, have wide ranges of coexistence in applied fields, and during the transformation process, it is impossible to destroy domains with kink-like structures even in high applied fields. The characteristic field H_α in the experiments may be explainable by such a process, which may involve skewed helices instead of flat helicoids. Most likely, transitions from a helicoid into free kinks and a transformation into a conical phase at higher fields takes place in many of the films. The first process is exactly the type of nucleation transition of helicoidal kinks, predicted by Dzyaloshinskii in his seminal work.[1] The second process seems to proceed by a domain process at higher fields.

The existence of a skyrmion lattice is a possible explanation for the unusual magnetization process and the unusual magnetic depth profiles from the PNR data. However, the magnetic anisotropy for the film with thickness $d = 26.7$ nm is found to be too low in the magnetic phase diagram (data point #2 in Fig. 2) in comparison to the theoretical threshold for stable skyrmion phases in the basic model, so that additional magnetic couplings would be required to stabilize such states. On the other hand, the demagnetizing field makes it difficult to transform a helicoidal or a conical structure into a phase with skyrmion axes running along the direction of an applied in-plane magnetic field.

Therefore, it is possible that in all experiments done so far, the skyrmion lattices are kinetically suppressed, although the estimated anisotropies of the MnSi films cover a range where the basic model displays thermodynamically stable skyrmions in applied fields, as shown in Fig. 2. There are clearly additional effects that may confound the formation of such a state and favor either the helicoidal order or other types of spiral order, even in equilibrium. A surface anisotropy may also be present with an *easy axis* that may distort any of these modulated phases. Moreover, it is possible that the isotropy of the Lifshitz invariants $\mathbf{m} \cdot \nabla \times \mathbf{m}$ is broken by the strain in the films since the DM interaction and the uniaxial anisotropy may have the same origin of a pairwise anisotropic exchange in a band ferromagnet.[49]

Based on the experimental observations, it is not possible to conclusively decide the question of which magnetic structures are responsible for the anomalous field-driven evolution in the experiments. It is clear that different MnSi films may even show different sequences of states. The fact that some films display two transitions at lower fields is suggestive of different magnetization processes. Be that as it may, a comparison of the magnetic profiles from the PNR data with depth profiles of the layer-averaged component of the magnetization in field direction $\langle M_x \rangle$ for different structures allows some conclusions on the possible magnetic modulations. Figure 13 shows profiles from numerical solutions to Eq. (1) that correspond to the 26.7-nm-thick film in a 0.5-T field reported in Fig. 9. The skewed anharmonic conical helix yields a good fit to the magnetic depth profile. In particular, the modulation falls short of the saturation magnetization in the negative direction. In contrast, $\langle M_x \rangle(z)$ of the flat helicoids covers the full range of the magnetization, from $+M_s$ to M_s, albeit with a strong anharmonicity. The distorted conical helix has constant value of magnetization in field direction. Finally, the profiles

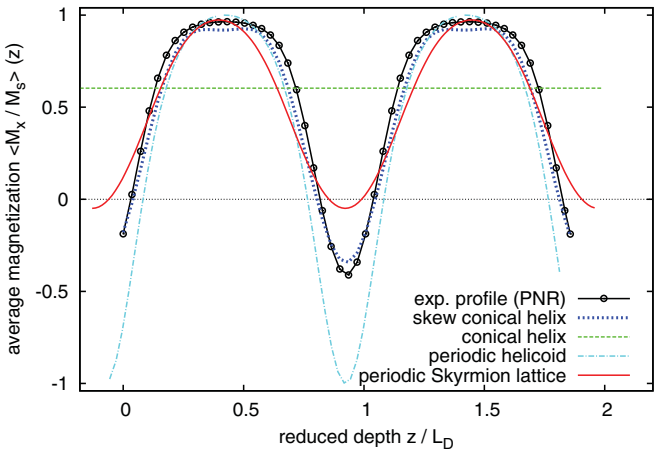

FIG. 13. (Color online) Experimental magnetization profile as normalized layer-averaged magnetization in field direction M_x vs position in the layer (normalized by wavelength of helix modulation) for the 26.7-nm-thick film in a 0.5-T field compared to numerical solutions for different modulated states. Data and solutions correspond to reduced anisotropy and field ($k = 0.04$, $h = 0.50$).

of the metastable and periodic skyrmion lattice solutions have a similar character as the experimental data. For the observations, we have then at least two possible explanations: (i) If one-dimensional modulations occur as intermediate states in the MnSi films, they should have a complex skewed conical structure. Additional magnetic couplings such as competing anisotropies would be required to explain such unusual helices in MnSi. (ii) A transverse distorted skyrmion phase does exist as a field-driven phase in easy-plane chiral magnets, as shown by the theoretical magnetic phase diagram. This explanation also requires additional magnetic couplings to achieve a quantitative agreement between the model and the experimental observations.

VI. CONCLUSION

The results of this work establish epitaxial MnSi films as a chiral cubic helimagnetic system where complex magnetization processes can be studied under the influence of induced magnetic anisotropies. The major part of this work shows that the in-plane tensile strain in MnSi(111) films produces an easy-plane uniaxial anisotropy, which can be explained by a homogeneous magnetoelastic effect. Both the theoretical results within a simplified model and the experiments reveal a number of modulated states that are metastable or do not exist in bulk MnSi, which is a nearly isotropic cubic helimagnet. Depending on the value of the uniaxial anisotropy, different types of magnetization processes are found. Our experimental data give clear indications for such processes in the MnSi films.

One of the most interesting transformation processes that may be observed in this system is the creation of solitonic states,[13] such as the nucleation of free kinks in the helicoidal phase in a transverse magnetic field, or alternatively the formation of skyrmion lattices. These structures have their own mesoscale lengths, fixed by the competition between Dzyaloshinskii-Moriya and direct exchange. This poses new problems for their stability and transformational behavior in confining geometries of magnetic nanostructures. Magnetic microscopic imaging now will play a major role in order to discriminate between the different chirally modulated states and to unravel the magnetic phase diagram relying on the intricate competition between these states. We also show that quantitative models for the magnetic behavior of these films will require very detailed determination of their magnetic properties, including higher-order anisotropies and surface effects.

ACKNOWLEDGMENT

This work was supported by the NSERC, the Canada Research Chairs Program, and DFG through Project No. RO 2238/9-1.

*theodore.monchesky@dal.ca

[1] I. E. Dzyaloshinskii, Zh. Eksp. Teor. Fiz. **47**, 992 (1964) [Sov. Phys. JETP **20**, 665 (1965)].
[2] P. Bak and M. H. Jensen, J. Phys. C: Solid State **13**, L881 (1980).
[3] B. Lebech, J. Bernhard, and T. Freltoft, J. Phys.: Condens. Matter **1**, 6105 (1989).
[4] A. N. Bogdanov and D. A. Yablonskii, Zh. Eksp. Teor. Fiz. **95**, 178 (1989) [Sov. Phys.–JETP **68**, 101 (1989)].
[5] A. N. Bogdanov and U. K. Rößler, Phys. Rev. Lett. **87**, 037203 (2001).
[6] U. K. Rößler, A. N. Bogdanov, and C. Pfleiderer, Nature (London) **442**, 797 (2006).
[7] A. N. Bogdanov, U. K. Rößler, and C. Pfleiderer, Phys. B (Amsterdam) **359**, 1162 (2005).
[8] X. Z. Yu, Y. Onose, N. Kanazawa, J. H. Park, J. H. Han, Y. Matsui, N. Nagaosa, and Y. Tokura, Nature (London) **465**, 901 (2010).
[9] X. Z. Yu, N. Kanazawa, Y. Onose, K. Kimoto, W. Z. Zhang, S. Ishiwata, Y. Matsui, and Y. Tokura, Nat. Mater. **10**, 106 (2011).
[10] S. Heinze, K. von Bergmann, M. Menzel, J. Brede, A. Kubetzka, R. Wiesendanger, G. Bihlmayer, and S. Blügel, Nat. Phys. **7**, 713 (2011).
[11] M. Bode, M. Heide, K. von Bergmann, P. Ferriani, S. Heinze, G. Bihlmayer, A. Kubetzka, O. Pietzsch, S. Blügel, and R. Wiesendanger, Nature (London) **447**, 190 (2007).
[12] A. Tonomura, X. Yu, K. Yanagisawa, T. Matsuda, Y. Onose, N. Kanazawa, H. S. Park, and Y. Tokura, Nano Lett. **12**, 1673 (2012).
[13] U. K. Rößler, A. A. Leonov, and A. N. Bogdanov, J. Phys.: Conf. Ser. **303**, 012105 (2011).
[14] J. Fukuda and S. Zumer, Nat. Commun. **2**, 246 (2011).
[15] N. S. Kiselev, A. N. Bogdanov, R. Schäfer, and U. K. Rößler, J. Phys. D: Appl. Phys. **44**, 392001 (2011).
[16] Y. Ishikawa, K. Tajima, D. Bloch, and M. Roth, Solid State Commun. **19**, 525 (1976).
[17] M. L. Plumer and M. B. Walker, J. Phys. C: Solid State **14**, 4689 (1981).

[18] A. I. Okorokov, S. V. Grigoriev, Y. O. Chetverikov, S. V. Maleyev, R. Georgii, P. Böni, D. Lamago, H. Eckerlebe, and K. Pranzas, Phys. B **356**, 259 (2005).
[19] S. Kusaka, K. Yamamoto, T. Komatsubara, and Y. Ishikawa, Solid State Commun. **20**, 925 (1976).
[20] K. Kadowaki, K. Okuda, and M. Date, J. Phys. Soc. Jpn. **51**, 2433 (1982).
[21] B. Lebech, P. Harris, J. S. Pedersen, K. Mortensen, C. I. Gregory, N. R. Bernhoeft, M. Jermy, and S. A. Brown, J. Magn. Magn. Mater. **140**, 119 (1995).
[22] S. V. Grigoriev, S. V. Maleyev, A. I. Okorokov, Y. O. Chetverikov, and H. Eckerlebe, Phys. Rev. B **73**, 224440 (2006).
[23] S. M. Stishov, A. E. Petrova, S. Khasanov, G. K. Panova, A. A. Shikov, J. C. Lashley, D. Wu, and T. A. Lograsso, J. Exp. Theor. Phys. **106**, 888 (2008).
[24] S. Mühlbauer, B. Binz, F. Jonietz, C. Pfleiderer, A. Rosch, A. Neubauer, R. Georgii, and P. Böni, Science **323**, 915 (2009).
[25] C. Pappas, E. Lelièvre-Berna, P. Falus, P. M. Bentley, E. Moskvin, S. Grigoriev, P. Fouquet, and B. Farago, Phys. Rev. Lett. **102**, 197202 (2009).
[26] H. Wilhelm, M. Baenitz, M. Schmidt, U. K. Rößler, A. A. Leonov, and A. N. Bogdanov, Phys. Rev. Lett. **107**, 127203 (2011).
[27] H. Wilhelm, M. Baenitz, M. Schmidt, C. Naylor, R. Lortz, U. K. Rößler, A. A. Leonov, and A. N. Bogdanov, J. Phys.: Condens. Matter (to be published).
[28] A. A. Leonov, A. N. Bogdanov, and U. K. Rößler, e-print arXiv:1001.1292.
[29] A. B. Butenko, A. A. Leonov, U. K. Rößler, and A. N. Bogdanov, Phys. Rev. B **82**, 052403 (2010).
[30] E. Karhu, S. Kahwaji, T. L. Monchesky, C. Parsons, M. D. Robertson, and C. Maunders, Phys. Rev. B **82**, 184417 (2010).
[31] E. A. Karhu, S. Kahwaji, M. D. Robertson, H. Fritzsche, B. J. Kirby, C. F. Majkrzak, and T. L. Monchesky, Phys. Rev. B **84**, 060404 (2011).
[32] E. Magnano, F. Bondino, C. Cepek, F. Parmigiani, and M. C. Mozzati, Appl. Phys. Lett. **96**, 152503 (2010).
[33] K. Schwinge, C. Müller, A. Mogilatenko, J. J. Paggel, and P. Fumagalli, J. Appl. Phys. **97** (2005).
[34] A. Hubert and R. Schäfer, *Magnetic Domains: The Analysis of Magnetic Microstructures* (Springer, Berlin, 1998).
[35] P. Bruno and J.-P. Renard, Appl. Phys. A **49**, 499 (1989).
[36] H. Fritzsche, J. Kohlhepp, and U. Gradmann, Phys. Rev. B **51**, 15933 (1995).
[37] B. Heinrich and J. F. Cochran, Adv. Phys. **42**, 523 (1993).
[38] W. J. M. de Jonge, P. J. H. Bloemen, and F. J. A. den Broeder, in *Ultrathin Magnetic Structures*, edited by J. A. C. Bland and B. Heinrich (Springer, Berlin, 1994).
[39] A. N. Bogdanov, U. K. Rößler, and K. H. Müller, J. Magn. Magn. Mater. **238**, 155 (2002).
[40] A. Thiaville and A. Fert, J. Magn. Magn. Mater. **113**, 161 (1992).
[41] D. Bloch, J. Voiron, V. Jaccarino, and J. H. Wernick, Phys. Lett. A **51**, 259 (1975).
[42] Y. Ishikawa, G. Shirane, J. A. Tarvin, and M. Kohgi, Phys. Rev. B **16**, 4956 (1977).
[43] S. V. Grigoriev, S. V. Maleyev, A. I. Okorokov, Y. O. Chetverikov, P. Böni, R. Georgii, D. Lamago, H. Eckerlebe, and K. Pranzas, Phys. Rev. B **74**, 214414 (2006).
[44] S. V. Grigoriev, V. A. Dyadkin, E. V. Moskvin, D. Lamago, T. Wolf, H. Eckerlebe, and S. V. Maleyev, Phys. Rev. B **79**, 144417 (2009).
[45] S. V. Grigoriev, S. V. Maleyev, V. A. Dyadkin, D. Menzel, J. Schoenes, and H. Eckerlebe, Phys. Rev. B **76**, 092407 (2007).
[46] C. Kittel, Rev. Mod. Phys. **21**, 541 (1949).
[47] U. Gradmann, J. Magn. Magn. Mater. **54-57**, 733 (1986).
[48] J. B. Staunton, S. Ostanin, S. S. A. Razee, B. L. Gyorffy, L. Szunyogh, B. Ginatempo, and E. Bruno, Phys. Rev. Lett. **93**, 257204 (2004).
[49] O. N. Mryasov, U. Nowak, K. Y. Guslienko, and R. W. Chantrell, Europhys. Lett. **69**, 805 (2005).
[50] J. B. Staunton, L. Szunyogh, A. Buruzs, B. L. Gyorffy, S. Ostanin, and L. Udvardi, Phys. Rev. B **74**, 144411 (2006).
[51] G. Wedler, J. Walz, A. Greuer, and R. Koch, Surf. Sci. **454–456**, 896 (2000).
[52] M. Komelj and M. Fähnle, Phys. Rev. B **65**, 092403 (2002).
[53] E. du Trémolet de Lacheisserie, *Magnetostriction: Theory and Applications of Magnetoelasticity* (CRC Press, Boca Raton, 1993).
[54] S. V. Maleyev, J. Phys.: Condens. Matter **21**, 146001 (2009).
[55] E. Fawcett, J. P. Maita, and J. H. Wernick, Int. J. Magn.**1**, 29 (1970).
[56] E. Franus-Muir, M. L. Plumer, and E. Fawcett, J. Phys. C: Solid State **17**, 1107 (1984).
[57] J. B. Staunton, Rep. Prog. Phys. **57**, 1289 (1994).
[58] T. Burkert, O. Eriksson, P. James, S. I. Simak, B. Johansson, and L. Nordström, Phys. Rev. B **69**, 104426 (2004).
[59] K. Koepernik and H. Eschrig, Phys. Rev. B **59**, 1743 (1999).
[60] J. P. Perdew, K. Burke, and M. Ernzerhof, Phys. Rev. Lett. **77**, 3865 (1996).
[61] The full relativistic option of the FPLO code, http://www.fplo.de, relies on an all-electron solution of the Dirac equation and incorporates spin-orbit coupling to all orders.
[62] T. Jeong and W. E. Pickett, Phys. Rev. B **70**, 075114 (2004).
[63] T. Moriya, *Spin Fluctuations in Itinerant Electron Magnetism* (Springer-Verlag, Berlin, 1985).
[64] Y. Ishikawa, T. Komatsubara, and D. Bloch, Phys. B & C (Amsterdam) **86**, 401 (1977).
[65] M. L. Plumer and M. B. Walker, J. Phys. C: Solid State **15**, 7181 (1982).